ORIGINAL ARTICLE

An Aerodynamic Assessment of Vehicle-Side Wall Interaction using Numerical Simulations

C. Read and H. Viswanathan*

Department of Engineering and Mathematics, Sheffield Hallam University, Howard Street, Sheffield, S1 1WB, United Kingdom,
Phone: +44 114 225 6244; Fax: +44 1142254449

ABSTRACT – The effects of induced pressure loads from a realistic vehicle onto the surface of a road-side wall are numerically investigated. Parameters such as vehicle speeds, vehicle-wall separation distances and the effects of inclined walls are examined to numerically characterise the vehicle-wall interactions. Aerodynamic characteristics such as the drag, lift, side forces and pressure co-efficients are analysed on the vehicle to provide a basis for comparison between each of the aforementioned variations. Our results demonstrate that a smaller separation distance between vehicle and wall enhances the pressure induced on both the wall and car which is found to be consistent with the experimental data published previously. We find that the presence of a wall in close proximity to the passing vehicle unfavourably influences the induced pressure on the side-wall and abruptly increases the drag, lift and side forces experienced by the vehicle. For a vertical side-wall, from a wall separation point of view, a separation distance of 1.35 normalised by the height of the vehicle tends to retrieve the cars' original drag and lift value. In addition, our results demonstrate that a wall inclined to the ground favourably influences the aerodynamic characteristics of the vehicle compared to its vertical counterpart.

INTRODUCTION

Induced pressure distribution is a common feature that occurs around all moving vehicles, whether influenced by another vehicle or a stationary object on the side of the road. The vehicle-induced aerodynamic loads additionally induce vibrations to some of the motorway sound barriers, since they are designed mostly taking into considering the natural wind loads and do not take into account the induced pressure loads from passing vehicles [1]. Initial studies on induced pressure on an overhead highway sign structure by vehicle-induced gusts were experimentally investigated by Cali and Covert [2] on a 1:30 scale. Their experiments revealed that the force induced on the sign was approximately 1/5th of the product of dynamic pressure based on the vehicle speed and area of the sign. Quinn et al. [3, 4] performed full-scale experiments that tested different plate structures and inclinations and corroborated the previous findings of Cali and Covert [4].

To-date, few studies exist in the literature on vehicle-wall interactions owing to the experimental challenges they pose in dynamic pressure measurements and due to computational complexities in accurately predicting the boundary layer interactions between the vehicle and the wall. Experimentally, wind tunnel tests on a 3/8th scale model race car by Wallis and Quinlan [5] showed abrupt changes in drag and lift forces when a race car passes in close proximity to a stationary wall. Strachan et al. [6] performed experimental investigations on an Ahmed body model [7] with backlight angles of 10°, 25° and 40° subjected to a free-stream velocity of 25 m/s with rolling road. Their results showed that by increasing the proximity to the wall enhances the drag on the Ahmed body models. Furthermore, their results evidenced the breakdown of longitudinal vortices on the near-wall side of the model as the wall-to-model distance decreases, and a large pressure drop is pronounced on the near-wall model side. Recently, Lichtneger and Ruck [8] have conducted full-scale experiments on various different vehicles in order to quantify vehicle specific pressure loads on the wall. These experiments revealed detailed pressure imprints on the wall that led to characteristic pressure patterns to classify the type of passing vehicle. Their experiments certainly form the motivation and basis for the computational effort demonstrated in this present work.

On the numerical front, to the best of authors' knowledge, only a handful of studies exist. Strachan et al. [9] have performed CFD simulations using RNG k-ε as well as the Reynolds Stress viscous models on an Ahmed body subjected to airflow in close proximity to the side-wall. Their findings reveal that the high Reynolds number model does not fully compare against their experimental findings and suggested further experimental investigation to ascertain whether the trends in flow velocity predicted by the CFD for the near wall vortex are mirrored by experimental data. Advantage CFD [10] have performed numerical investigations using a 1/3rd Gen 4 NASCAR model with only one wall separation distance. By observing the pressure contours, they concluded that the vehicle experienced high lift at the front end towards the side-wall. Wang et al. [11] attempted numerical simulations on highly simplified commercial vehicles using the Realizable k-ε and RNG k-ε turbulence closures. A point source comparison on pressure was reported suggesting a good agreement between model and experiment. However, the imprint on induced wall pressure profile as such was not

reported. Their results, however, suggested that the shorter vehicle would produce a larger negative pressure peak. The effects of vehicle-wall interaction especially from the vehicle's aerodynamic coefficients were not investigated in the analysis of Wang et al. [11]. Also, a calibration of the model in terms of vehicle shape was not carried out. Most recently, Uddin et al. [12] investigated the flow over a 25° slant angled Ahmed body next to a side wall using STAR-CCM+ software. Using an "over-set" grid approach, they used an SST γ-Reθ transition model in predicting the flow and further compared their results using the SST model and that obtained using the AKN k-ε model with low-Re damping function. Their findings suggest that with a vehicle-wall separation larger than 1.3 times the width of the car, the force coefficients revert to the isolated body values.

From reviewed literature, it can be inferred that there is a significant lack of numerical understanding of the aerodynamic forces induced on realistic cars and side walls, their separation distances and inclination to ground. The current effort is targeted at (i) numerically representing a realistic model that was experimentally investigated by Lichtneger and Ruck [8], (ii) predict the induced pressure loads and aerodynamic forces by studying wall inclined at 10° to the ground. Prior to doing this, we carefully evaluate different eddy viscosity turbulence closures and establish grid independency for the numerical accuracy of the proposed models.

SIMULATION METHODOLOGY

The schematic of the model used in the present investigation is shown in Figure 1. Three separation distances between the car and the wall namely, 0.5m, 1m, and 2m and additionally a wall inclined at 10° away from the ground plane are considered. From a vehicle speed perspective, two inlet velocities were considered namely 50 mph and 60 mph that correspond to Reynolds numbers (Re$_H$) 2.2x10^6 and 2.6x10^6 respectively based on the height of the vehicle shown in Figure 1. In accordance with the original experiment, the car was located 15 m behind the start of the wall toward the stream-wise direction that corresponds to 3.2L, where L is the length of the vehicle which is 4.7 m as shown in Figure 1(a). This location was chosen in the present simulation to replicate the experimental setting where pressure measurements were originally positioned in the experiment [8].
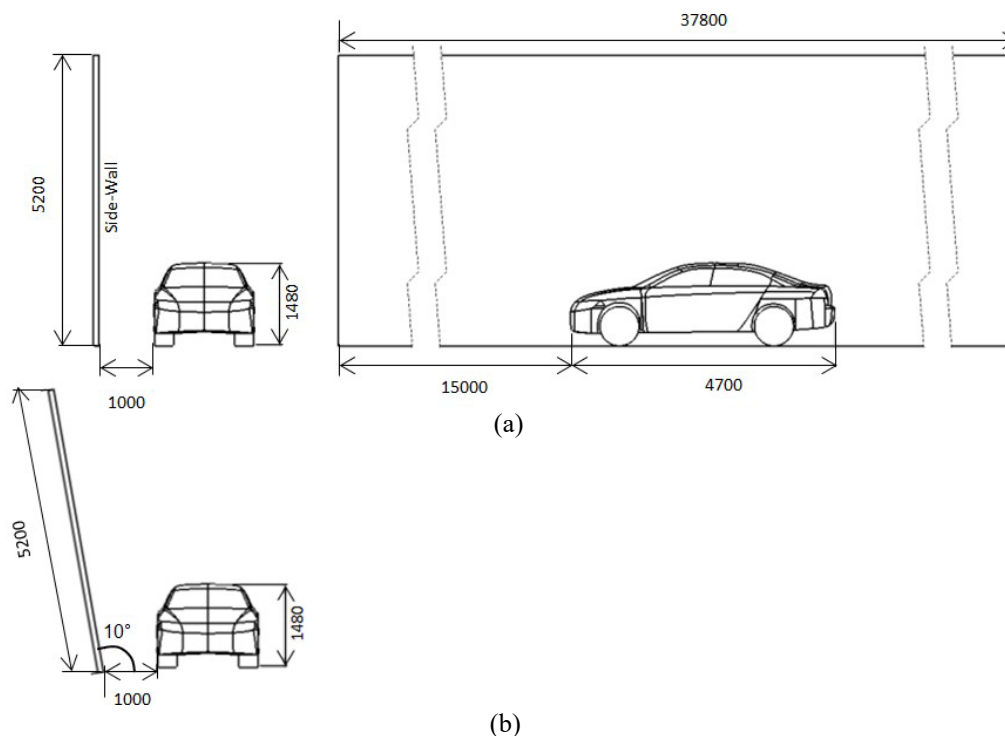

Figure 1. Assembly layout of the vehicle showing (a) a vertical wall with 1 m separation distance and (b) a wall inclined at 10° at a separation distance of 1 m from the ground.

The vehicle used in the present computational study is shown in Figure 2(a) is based on a simplified model of the Volkswagen Passat (VW Passat CC) that was investigated as the vehicle "type 1" in the experimental data of Lichtneger and Ruck [8]. Using SolidWorks (Ver. 2018), a CAD model was developed from the available blueprints of VW Passat CC to correctly represent the intricate surface features [13]. The details of the computational domain used for the CFD simulation, boundary conditions along with the wall and vehicle are shown in Figure 2(b).

The overall computational domain size is based on ERCOFTAC guidelines [14, 15] and was reasonably large to adequately capture the flow with minimal blockage effects.
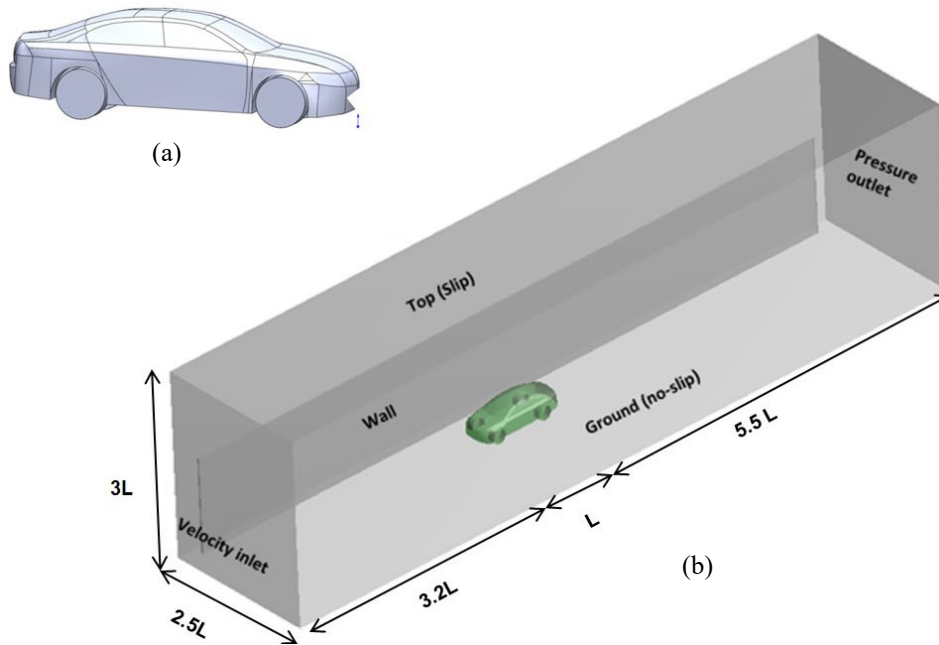
Figure 2. (a) A simplified CAD model of a Volkswagen Passat (CC) and (b) computational domain in 3D with boundary conditions.

Turbulence Modelling

In the present study, the analysis was carried out using a commercial code ANSYS Fluent (Ver. 18.1). For realistic car models, several previous evaluations have shown that the two-equation k-ε turbulence closures have been successful in reasonably describing the aerodynamics properties on commercial vehicles [16-19] and more serve as a popular choice for Industrial flows [24, 25]. Therefore, in this study, the two-equation turbulence models, namely the Standard k-ε and Realizable k-ε were considered and in addition, the one equation Spalart-Allmaras model was considered in further assessing the appropriateness of the predictions from the two-equation turbulence closures. Another choice of modelling is perhaps the RNG k-ε model which has shown superior performance to Standard k-ε. However, it must be emphasized that neither the Standard k-ε nor the RNG k-ε model which is suited to highly strained internal flow is realizable. The difference between the Realizable k-ε and Standard k-ε turbulence models is based on the approach through which the eddy viscosity is computed. The modelled eddy viscosity is given by:

$$\mu_t = \rho C_\mu \frac{k^2}{\varepsilon} \tag{1}$$

where ρ corresponds to density, k and ε correspond to kinetic energy and dissipation rate respectively. In the case of Standard k-ε model, the value C_μ=0.09 whereas, for the Realizable k-ε model it is no longer a constant but instead formulated as a function of mean strain rate tensor, mean rotation rate tensor and field variables of turbulence namely, the turbulence kinetic energy k and the dissipation rate ε is given as follows:

$$C_\mu = \frac{1}{A_0 + A_s \frac{kU^*}{\varepsilon}} \tag{2}$$

where U^* is given by

$$U^* = \sqrt{\left(S_{ij}S_{ij} + \widetilde{\Omega}_{ij}\widetilde{\Omega}_{ij}\right)} \tag{3}$$

With

$$S_{ij} = \frac{1}{2}\left(\frac{\partial u_j}{\partial x_i} + \frac{\partial u_i}{\partial x_j}\right) \tag{4}$$

where S_{ij} and $\widetilde{\Omega}_{ij}$ represent the mean strain rate tensor and mean rate of rotation tensor in a moving reference frame with the angular velocity of ω_k respectively. Also,

$$\widetilde{\Omega}_{ij} = \Omega_{ij} - 2\epsilon_{ij}\omega_k$$
$$\Omega_{ij} = \widetilde{\Omega}_{ij} - \epsilon_{ij}\omega_k \tag{5}$$

Additionally, the model constants A_0 and A_s are given by:

$$A_0 = 4.04$$

$$A_s = \sqrt{6}\,\cos\varphi \tag{6}$$

where

$$\varphi = \frac{1}{3}\cos^{-1}(\sqrt{6}\,W), W = \frac{S_{ij}S_{ik}S_{ki}}{\tilde{S}^3}; \ \tilde{S} = \sqrt{S_{ij}S_{ij}} \tag{7}$$

The above formulation for C_μ shall tend to satisfy the mathematical constraints imposed on Reynolds stresses consistent with turbulent flows.

Grid Resolution Check

A grid evaluation study was carried out for $Re_H = 2.6 \times 10^6$ for all the aforementioned turbulence models. However, this evaluation was carried out by neglecting the presence of the side wall. The side wall was disregarded for this study so that we could assess both the accuracy of turbulence models and the grid chosen by comparing the reported drag coefficient (C_d) on the vehicle from the literature [20] which is very much in agreement with experimentally reported values of Kounenis et al. [21] for a Volvo S60 vehicle and Heft et al. [22] for DrivAer Fastback models which suitably represent both the vehicle topology [23] and Reynolds numbers investigated in the present work. The definitions of the aerodynamic force coefficients used in the present study namely, the drag force coefficient (C_d), the lift force coefficient (C_l) and the side force coefficient (C_s) are summarised as follows:

$$C_d = \frac{F_d}{\frac{1}{2}\rho V^2 A_f}, C_l = \frac{F_l}{\frac{1}{2}\rho V^2 A_f}, C_s = \frac{F_s}{\frac{1}{2}\rho V^2 A_f} \tag{8}$$

where F_d, F_l and F_s are the aerodynamic drag, lift, and side forces respectively. A_f is the projected frontal area of the vehicle and V corresponds to the inlet velocity based on the Re_H values used in the present study.

The choice of the grid such as the tetrahedral, hexahedral, and polyhedral are subjective to various parameters such as the solver, the type of turbulence model and available computational resources etc. but without compromising accuracy. In this case, the grid chosen for this study is constructed entirely using unstructured hexahedral elements based on "Cut-Cell" methodology from ANSYS Meshing. By maintaining the same surface sizes and element quality and the boundary layer resolution as the hexahedral mesh, a tetrahedral mesh is found to increase the element count by a factor of 4. The total height of the boundary layer was defined as the wall-normal distance to a point where the flow reaches 99% of the free-stream velocity V. An estimate of the thickness of the boundary layer (δ) at any point x at the boundary was obtained using the one-seventh power law; $\delta = 0.16x/Re_x^{1/7}$. A specified, desired wall $y^+=50$ over the surface of the car was preserved. Maintaining a $y^+=1$ for a realistic vehicle like ours, enhances the mesh count to > 5 times as to what is presented and may well be suitable for low-Re turbulence closures such as the SST k-ω model. Once again, we would like to recall that the focus of our work focusses on high-Re turbulence models variants including the SA and SKE and RKE, so the mesh determined for grid evaluation is consistent as well. The numerical solution is obtained by choosing the SIMPLE pressure-velocity coupling scheme together with the Second Order Upwind scheme for spatial discretization of equations for pressure, momentum, turbulence kinetic energy, and turbulence dissipation rate.

For each of the simulated cases within the two-equation turbulence models, the convergence in the solution was assessed by monitoring the residuals of the aforementioned equations dropping below 1×10^{-5} and with all simulations attaining a drag value deviation of less than 1%. However, with the Spalart-Allmaras model, the drop in residuals obtained was limited to values $<1 \times 10^{-4}$ by simulating over 5000 iterations; beyond which, both the residuals and monitored drag coefficient remained saturated. Figure 3a shows streamline plot with velocity vectors at the mid-plane of the vehicle in streamwise direction for the models mentioned above with $Re_H = 2.6 \times 10^6$. With reference to the Realizable k-ε model (Figure 3a (ii)), the Spallart-Allmaras model (Figure 3a (i)) appears to show stronger separation near the wake region with stronger streamline curvature adjacent to the deck. Whereas, the standard k-ε model (Figure 3a (iii)) tends to show the near wake streamline distributions more in-line with the Realizible k-ε model, it predicts lower velocity distribution under the boot-deck. Additionally, as shown in Figure 3b, the Realizable k-ε model with a standard wall treatment and with a grid of ~4.66 million cells gives a reasonably close match with the findings from the literature [20]. Therefore, the Realizable k-ε model was adopted for all simulations executed in the present study.

However, with the addition of wall and its variants, the mesh count increased remaining between ~5.28-5.90 million cells for the simulations carried out in the present study. An illustration of the mesh type and the overall grid distribution adopted with the presence of side-wall is shown in Figure 4. All computations were carried out using HP Z820 workstation with Intel Xeon E5-2660 V2, 40 thread-processors with a total RAM of 192 GB.
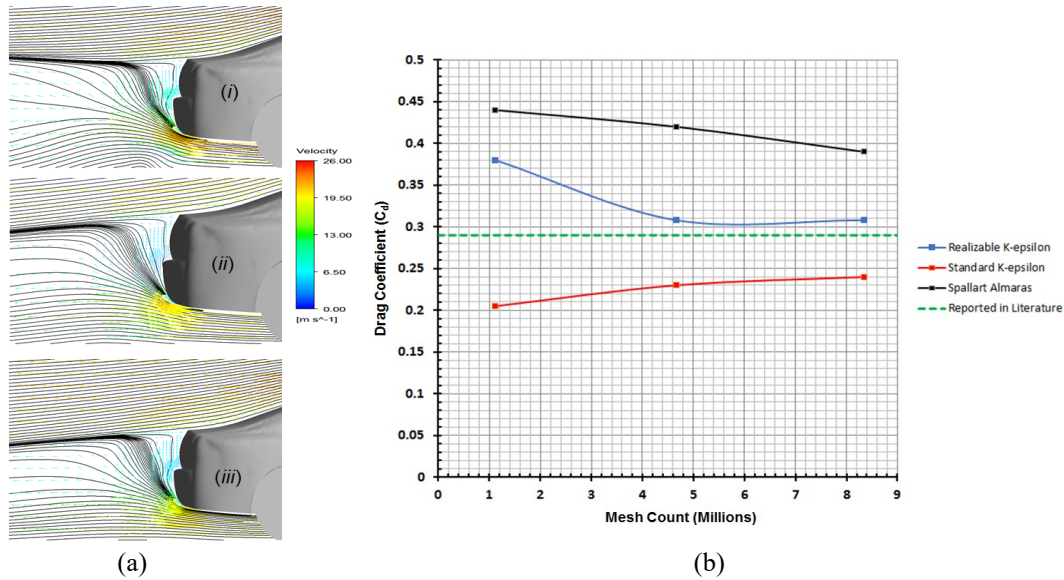
(a)

(b)

Figure 3. Mesh dependency study and evaluation of turbulence models evaluated in the present work. In Figure (a) parts (*i-iii*) represent the Spallart-Allmaras, the Realizable k-ε model, and the Standard k-ε model respectively. Figure (b) shows drag coefficients from various turbulence models compared against value reported in the literature [20].
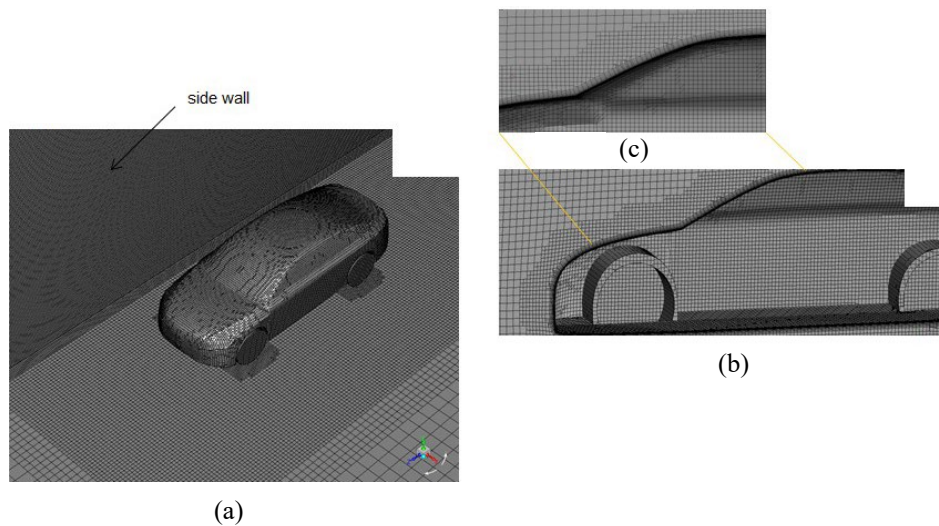

(a)

(c)

(b)

Figure 4. Cut-cell mesh used in the present study showing (a) the regions of surface refinements, (b) a cut section of volume cell distribution and (c) with boundary layer details over the car.

RESULTS

The results from the simulations are discussed with respect to validation simulation results with experimental data for pressure imprints on the side wall, the influence of vehicle- wall separation distances and the inclined wall on the overall flow features and the aerodynamic forces over the vehicle. In this section, we present our numerical results in parts that are focused to fully evaluate vehicle-wall interaction, namely: (i) a comparison with experimental data for pressure imprints on the side wall, (ii) the effect of vehicle-wall separation distances, (iii) the effect of an inclined wall in relation to its vertical counterpart. Finally, a summary of the aerodynamic coefficients influenced on the vehicle due to the presence of the wall and its variants are presented. To characterise the pressure imprints on the side wall, the coefficient of pressure (C_P) from the simulation is compared against the experimental data from previously published results of Lichtneger and Ruck [8] as shown in Figure 5. The pressure coefficient is defined as follows:

$$C_P = \frac{P - P_{ref}}{\frac{1}{2}\rho V^2} \tag{9}$$

where P and P_{ref} correspond to the calculated mean pressure and reference pressure respectively.

Comparison with Experimental Data

It was established in the experimental data of Lichtneger and Ruck [8] that vehicles of this size tend to have one suction zone as seen in Figure 5(a) whilst longer vehicles tend to show two suction peaks. Figure 5(b) shows the results predicted by the present simulations wherein, the overpressure zone at the front end of the vehicle tends to have a good qualitative as well as quantitative match with the experimental data. At the rear end, the experimental data shows that the pressures do not reach values as high as that seen in the front; which is reasonably predicted by the model overall but quantitative as well as qualitative some discrepancies are evidenced in comparison with the experiments at the rear.

Qualitatively, the contours of pressure distribution are very encouraging in the zone of the vehicle where the suction peak is present. However, the model does not quantitatively replicate the sharp suction peak seen in the experimental results unlike the agreement seen in the overpressure regions. Considering that the model has been simplified in terms of the vehicle geometry, that the results are a representation of a time-independent simulation, at this juncture, we emphasize that a direct comparison or a comparison at equivalent levels with the experimental result is rather challenging. However, despite such differences, we see that the characteristic pressure imprints predicted by the simulation are encouraging in relation to that determined experimentally.
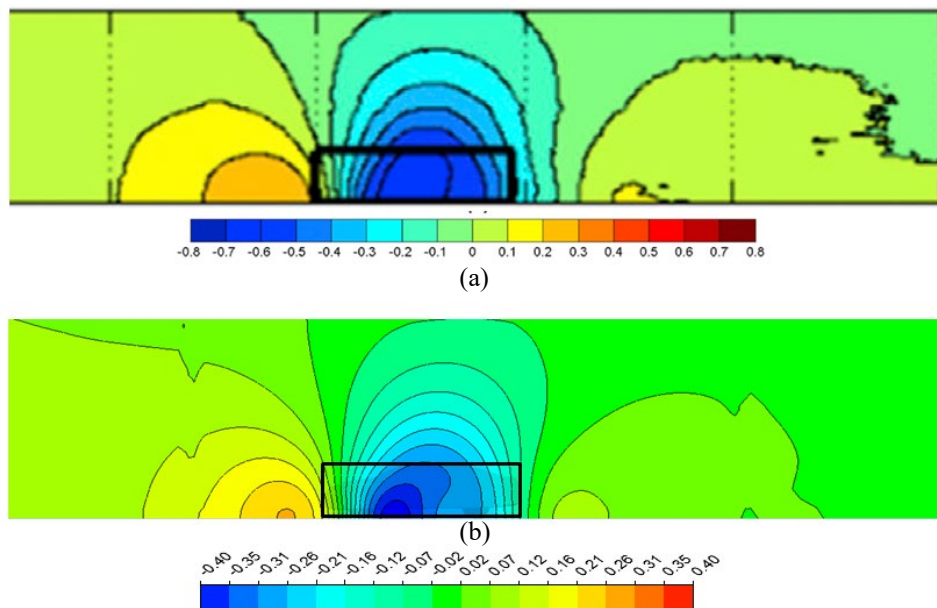

Figure 5. Characteristic pressure imprints on the side wall (C_P): The image (a) is obtained from published work of Lichtneger and Ruck [8] and image (b) shows predictions from the present numerical work carried out with $Re_H = 2.6 \times 106$, for a vehicle-wall separation distance of 1 m.

(Reprinted from Journal of Wind Engineering and Industrial Aerodynamics, 174, P. Lichtneger & B. Ruck, Full scale experiments on vehicle induced transient pressure loads on roadside walls, 451-457, Copyright (2018), with permission from Elsevier)

Effect of Vehicle-Wall Separation Distance

Figure 6 shows the static pressure distribution at the upstream, extracted at a plane 0.5 m in front of the vehicle. The profiles of static pressure distributions are markedly different in their shape and show asymmetric pressure distribution patterns as one would expect due to the side wall's presence. It can be seen that the overpressure predicted at the centre of the vehicle's symmetry gradually decreases with an increase in wall separation distance and for a separation distance of 2 m shown by Figure 6(c), the distribution pattern and the peak pressure distribution values appear to be in close agreement with the vehicle only case as shown in Figure 6(d). We see a recovery with pressure distribution that tends to become symmetric for a separation distance of 2 m and matching closer to that exhibited by the case where no wall was present.

The wall pressure imprints due to varying vehicle-wall separation distances are presented in Figure 7 for $Re_H = 2.2 \times 10^6$. We observe that at a separation distance of 0.5 m shown by Figure 7(a), where one large suction zone is evident on the wall within the vicinity of the vehicle; at the rear three distinct zones are evidenced. A narrower, but a weaker suction zone a_2 which appears nearly sandwiched between two overpressure zones a_1 and a_3 of which, a_1 appears stronger. With increasing vehicle-wall separation distances such as for 1 m and 2 m shown in Figures 7(b) and 7(c), the pressure imprints at the rear do not show a presence of a mild suction zone unlike that seen in Figure 7(a).

It is important to highlight that for all the cases shown in Figure 7, the imprints show the same trend on the wall in terms of predicting an over-pressure zone at the front and the presence of one suction zone within the vicinity of the vehicle as pronounced by the experiments for the class of vehicle examined in this study. Also, the results show a general trend that appears intuitive wherein, the magnitude of these pressure zones decreases with increase in vehicle-wall separation distance. Furthermore, an interesting comparison is to verify the effect of vehicle speeds for the same separation distances. For vehicle speeds examined in this study, we see that for a slower vehicle speed shown in Figure 5(b), the

overall magnitude of the aforementioned pressure zones reduces in comparison to Figure 7(b) besides, the overall characteristic imprints on the wall show negligible differences.
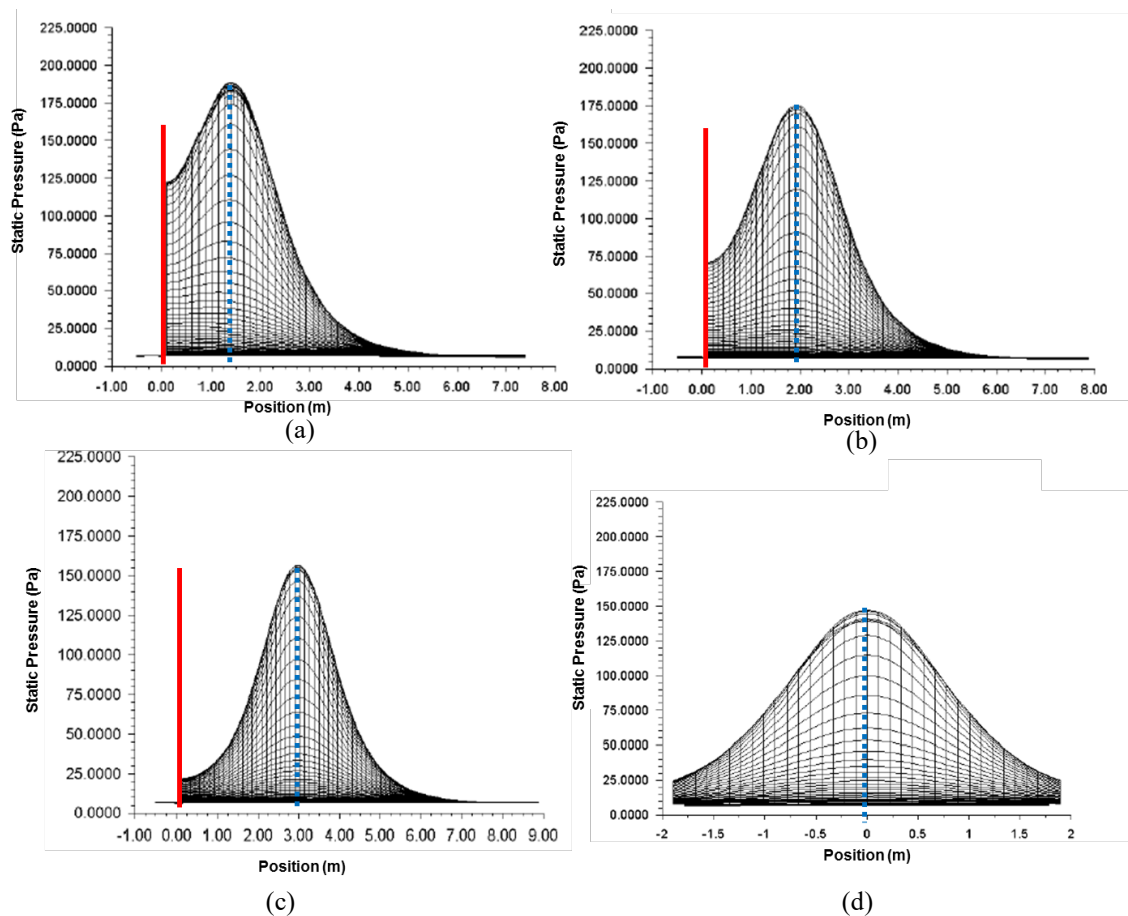

Figure 6. Static pressure distribution from the simulations at a plane located at 0.5 m in front of the vehicle with Re_H = 2.6×10^6: The red line shows the location of the side-wall and the dotted blue line indicates the centre of the vehicle. The vehicle-wall separation distances shown in images (a), (b), (c) correspond to 0.5 m, 1 m, and 2 m respectively from the vehicle whereas, the image (d) shows the result for a vehicle only case.

In Figure 8 we analyse the velocity streamlines at the mid-section extracted in the span-wise direction together with the distribution of (C_P) viewed from the rear of the vehicle. For Figures 8 (a) to 8(c), wall distances are increased from 0.5 m to 2 m respectively and the presence of a wall is indicated as a red-strip whereas, the Figure 8(d) shows results from the simulation executed for a vehicle the only case where the presence of side-wall is neglected. At least two important observations are evident from Figure 8 namely: (i) with the vehicle closer to the wall (Figures 8(a) and 8(b), the region between the vehicle and the wall experiences flow that are directed upwards suggesting sharp increments potentially in the lift and side forces whereas with a 2 m separation distance (see Figure 8c), the curvature in streamlines seem to be less influenced by the wall providing a closer agreement with Figure 8d tending to behave like the vehicle only case. Additionally, (ii) for closer vehicle-wall interactions, (C_P) over the rear of the vehicle shows an asymmetric distribution with larger suction regions present that gradually tend to appear like the vehicle only case when the separation distance is increased. This is further evidenced by the distribution of (C_P) on the side of the vehicle near the wall shown in Figure 9.

The velocity streamlines are shown at the symmetry plane of the vehicle in the stream-wise direction with varying vehicle-wall distances such as 0.5 m, 1 m and 2 m in Figures 9 (a) to 9(c) whereas, for Figure 9(d), the vehicle only case is presented. The near-wake distribution for all the cases presented does not show trends that are strikingly different. However, in summary, the (C_P) on the vehicle upholds the same trend presented in Figure 8 showing a larger distribution of the suction regions for smaller vehicle-wall separation distances which gradually transform into regions of high pressure with increasing separation distance. This suggests that the vehicle could potentially experience abrupt changes in its aerodynamic characteristics when it passes closer to the wall.
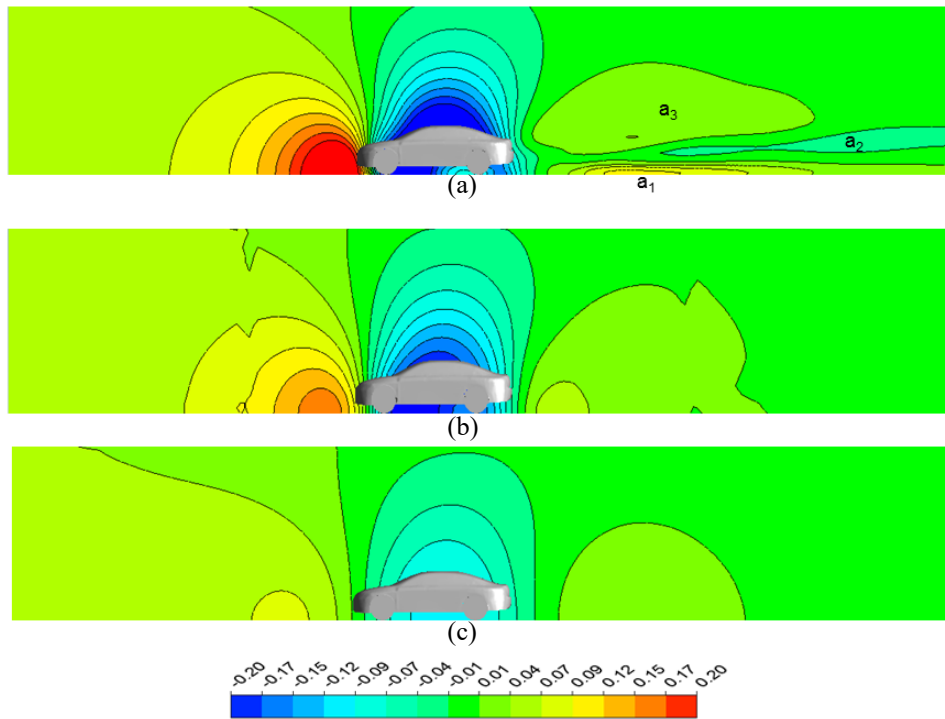
Figure 7. Numerical results of characteristic pressure imprints on the side wall (C_P) for vehicle-wall separation distances of (a) 0.5 m, (b) 1 m and (c) 2 m respectively for $Re_H = 2.6 \times 10^6$.
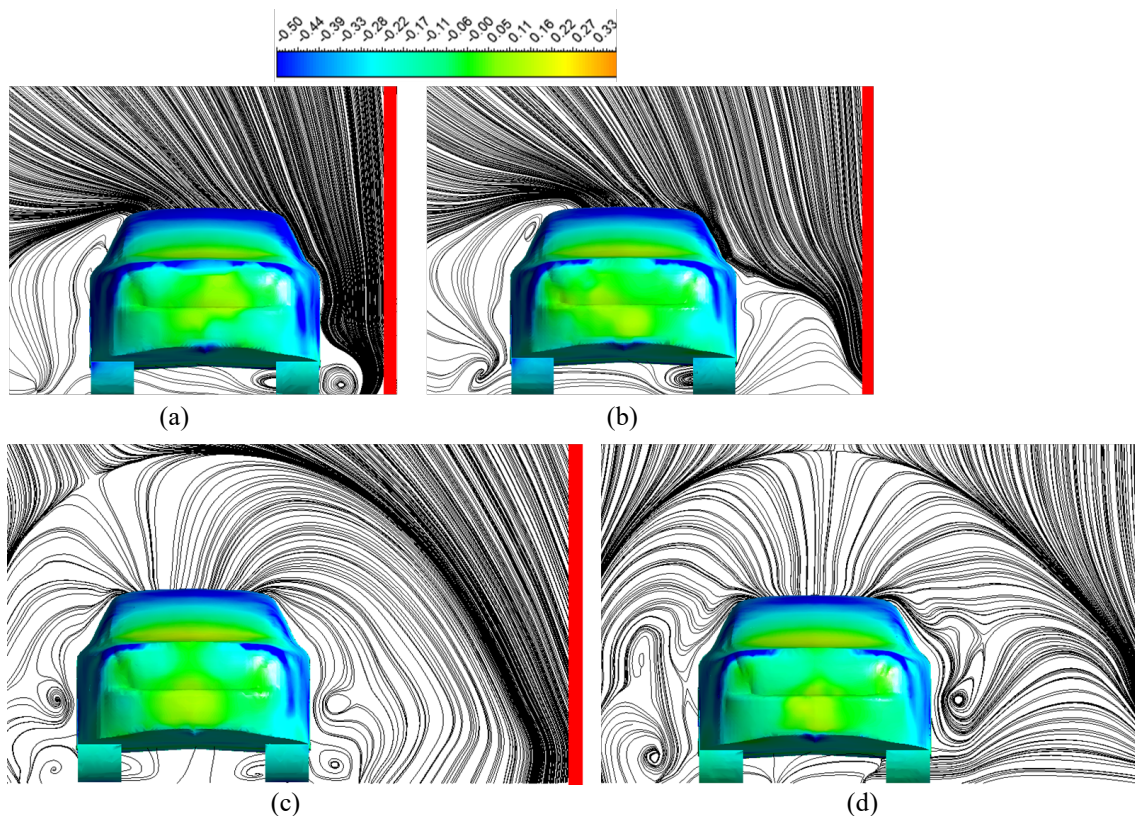

Figure 8. Rear view of the vehicle showing the (C_P) distribution and velocity streamlines extracted at the mid-plane of the vehicle in span-wise direction for vehicle-wall separation distances of (a) 0.5 m, (b) 1 m and (c) 2 m respectively and (d) vehicle only case for $Re_H = 2.6 \times 10^6$. The location of the side wall is indicated as a red-strip.
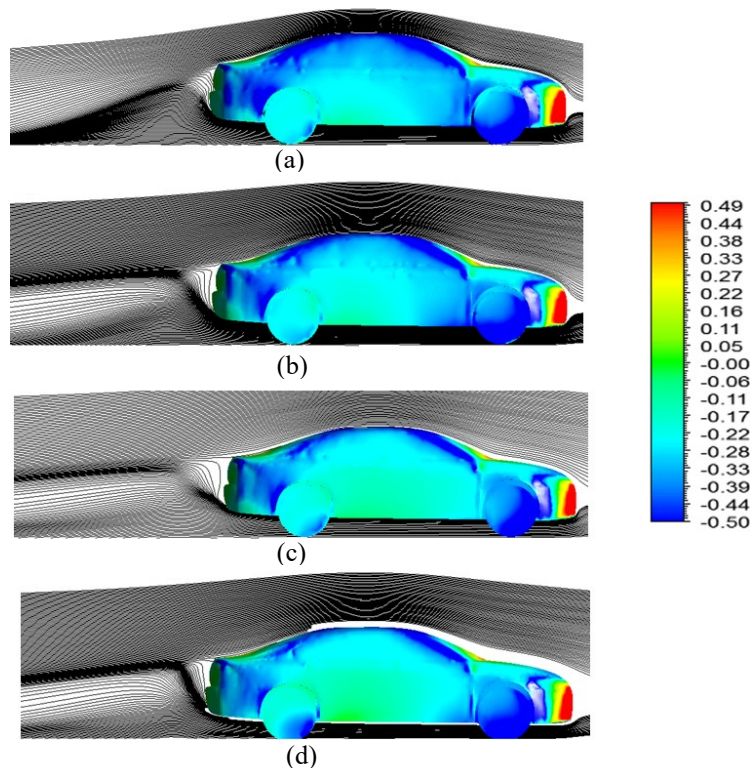
Figure 9. View of the vehicle side next to the wall showing the (C_P) distribution and velocity streamlines extracted at the symmetry plane of the vehicle in stream-wise direction for vehicle-wall separation distances of (a) 0.5 m, (b) 1 m and (c) 2 m respectively and (d) vehicle only case for $Re_H = 2.6 \times 10^6$.

Effect of an Inclined Side-Wall

In this section, we present the numerical results for an inclined wall shown in Figure 1b which is then compared against its vertical counterpart shown in Figure 1a. Figure 10 shows the static pressure distribution at the upstream, extracted at a plane 0.5m in front of the vehicle for simulations with a vertical wall and for inclined wall respectively. It can be seen that the inclined wall shown by Figure 10b has a reduced peak pressure distribution in the front and in the region between vehicle and wall in comparison to the vertical wall shown by Figure 10a. Also, in the region between vehicle and wall, an asymmetry in overall pressure distribution that is strongly evidenced in both the span-wise and in the vertical directions for an inclined wall.
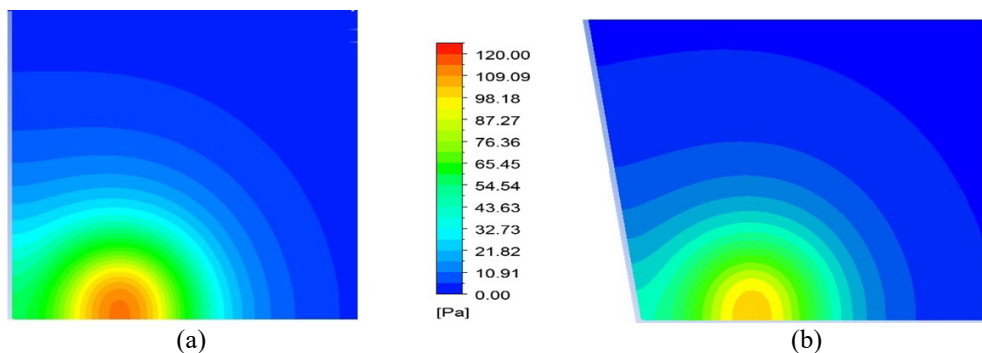

Figure 10. Static pressure distribution from the simulations at a plane located at 0.5 m in front of the vehicle with $Re_H = 2.2 \times 10^6$ for a vehicle wall separation distance of 1 m. The location of the side-wall is shown by the grey strip on the left. Image (a) shows the results for a vertical wall and (b) shows the result for a wall inclined at 10° to the ground.

A comparison of the pressure imprints (C_P) between the vertical wall and its inclined counterpart is shown in Figure 11(a) and 11(b). For an inclined wall, at vertical distances away from the vehicle the pressure imprints appear to be mitigated in comparison to the vertical wall. This result appears quite intuitive because, with an increase in height, the vehicle-wall separation distance increases and due to wall inclination one would expect lesser interference between the vehicle and wall at larger heights. However, closer to the ground where the vehicle-wall distance between the inclined wall and its vertical counterpart are alike, we observe a significant reduction in the over-pressure zone in the front, a reduction in the suction zone at the vicinity of the vehicle and a noticeably different contour that is tail-like at the rear.
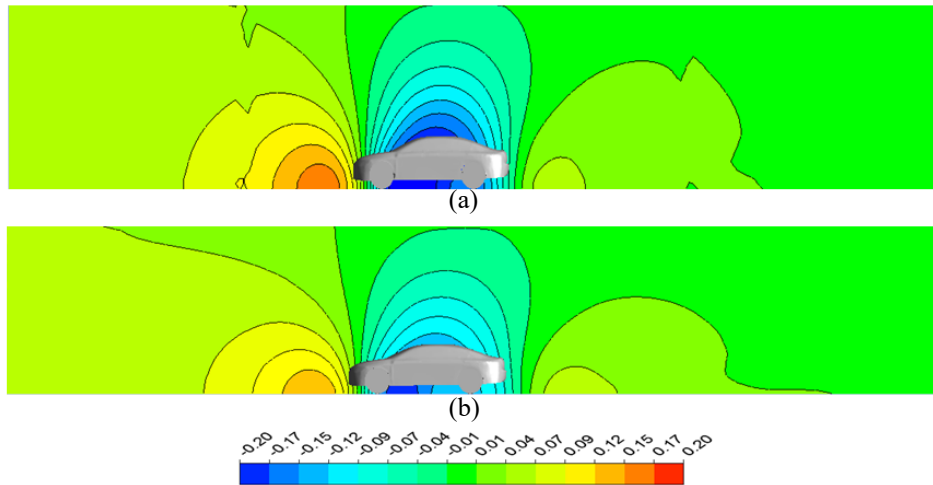
Figure 11. Numerical results of characteristic pressure imprints on the side wall (C_P) for vehicle-wall separation distances of 1 m, with $Re_H = 2.2 \times 10^6$ for (a) a vertical wall and (b) a wall inclined at 10°.

Figure 12(a) and 12(c) show the (C_P) profiles plotted at the rear along with the velocity streamlines at the mid-plane of the vehicle whereas the Figure 12(b) and 12(d) show the velocity vector plots with magnitude for vertical and inclined walls respectively. It is evident that the (C_P) distribution adjacent to the inclined wall is dominated by the overpressure zones; this is also evidenced in the Figure 13(a) and 13(c) where (C_P) is extracted at the side of the vehicle closer to the wall. The velocity magnitude shown by Figure 12(b) and 12(d) suggest the flow experienced over the side of the vehicle is less prominent with the inclined wall compared to the vertical wall and lift experienced by the vehicle closer to the C-pillar is more dominant with a vertical wall. The streamlines shown by Figure 13 in the symmetry plane of the vehicle in the stream-wise direction indicate that the there is a potential change in the near wake structure for the vehicle closer to the inclined wall shown by Figure 13(a) and 13(b) than compared to its vertical counterpart shown in Figures 13(c) and 13(d).

For all the aforementioned investigations, the numerical results suggest that the vehicle that passes closer to the inclined wall is clearly advantaged over that passes next to its vertical counterpart. Finally, we present a comparison summary of the aerodynamic coefficients in Table 1 for cases with variations in vehicle-wall separation distances, for the inclined wall and for the vehicle only case where the presence of the wall was neglected. The values presented in Table 1 suggest that the forces experienced by the vehicle at a wall distance of 2 m, which is potentially 1.35 times the height of the vehicle examined in this study, a significant recovery with all the aerodynamic forces experienced by the vehicle. For the case of an inclined wall when compared to its vertical counterpart, an advantage with the aerodynamic forces experienced by the vehicle in all aspects are evidenced, however, a reduction in the side force predicted does not seem to be significant.
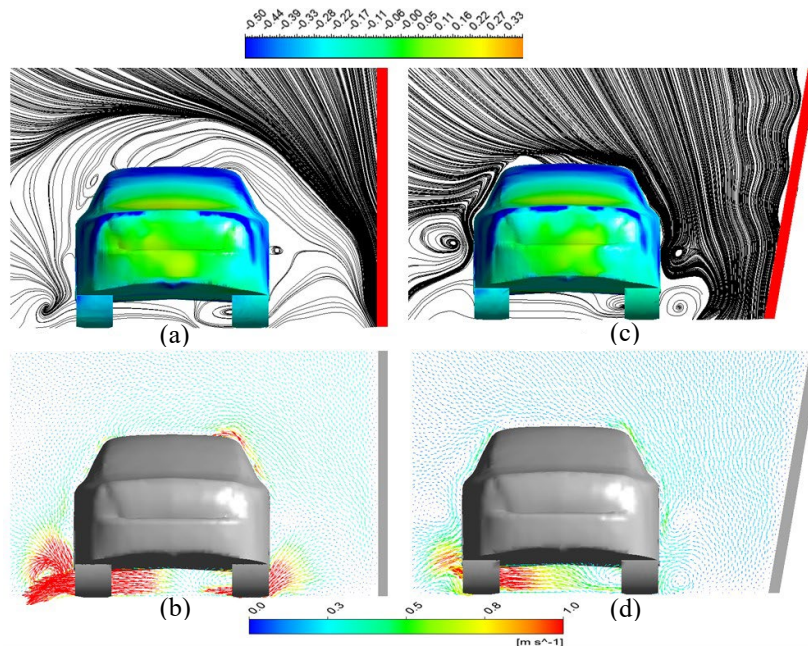

Figure 12. Rear view of the vehicle showing (a) the (C_P) distribution and velocity streamlines and (b) the magnitude of velocity vector extracted at the mid-plane of the vehicle in span-wise direction for a vertical wall. The images (c) and (d) correspond to the wall inclined at 10°. The results are executed for $Re_H = 2.2 \times 10^6$.
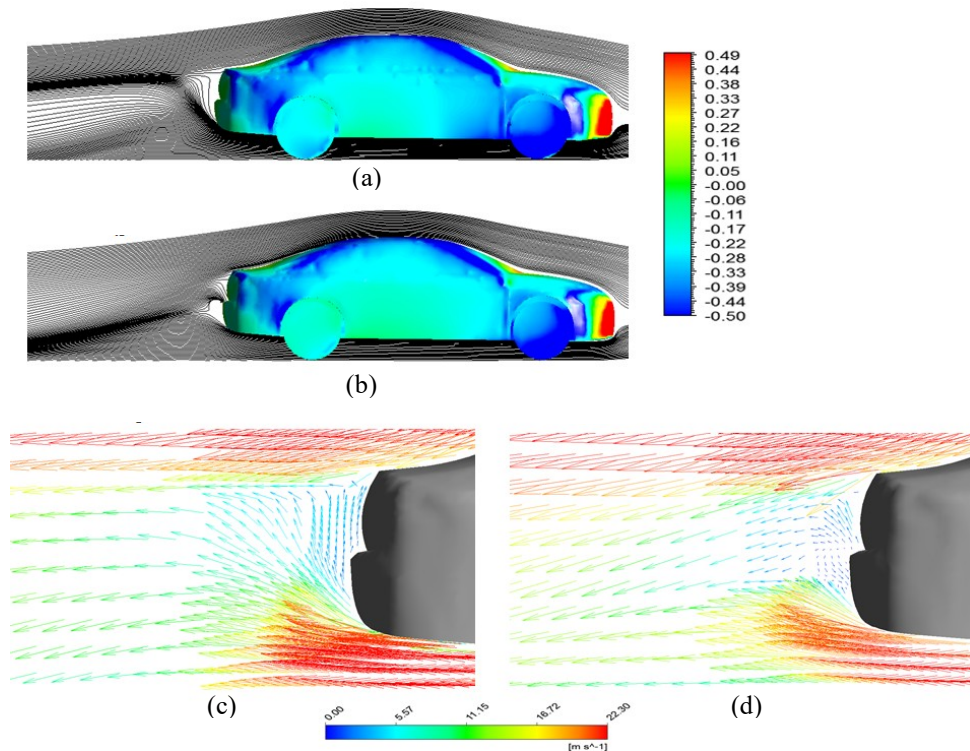
Figure 13. View of the vehicle side next to the wall showing the (C_P) distribution and velocity streamlines extracted at the symmetry plane of the vehicle in stream-wise direction for (a) vertical wall and (b) wall inclined at 10°. The images (c) and (d) correspond to the magnitude of velocity vectors corresponding to images (a) and (b) respectively. The results are executed for $Re_H = 2.2 \times 10^6$.

Table 1. Aerodynamic coefficients on the vehicle for various vehicle-wall proximity distance for $Re_H = 2.6 \times 10^6$.

Sc.no	Vehicle-Wall proximity distance	C_d	C_l	C_s
1	0.5m	0.3810	0.3622	0.05878
2	1 m	0.3468	0.2979	0.03568
3	a wall inclined at 10° to the ground at 1m proximity from the vehicle.	0.3370	0.2906	0.02320
4	car only simulation (neglecting the presence of a wall)	0.3083	0.2780	0.00930
5	2 m	0.3129	0.2815	0.0181

CONCLUSION

Aerodynamics of vehicle-wall interactions is vital to automotive and transportation engineering for various reasons such as, but not restricted to vehicle identification, design of barriers in highways, and provides a deeper understanding of the driver behaviour and vehicle design. In this paper, we have presented a comprehensive analysis of the aerodynamic interaction between a saloon type vehicle and the wall adjacent to it. As a rationality check, by neglecting the presence of a wall, we numerically establish the drag on the vehicle by comparing different turbulence models and mesh sizes and find that the result predicted by the Realizable k-ε turbulence model which matched closely with that reported in the literature. From a vehicle-wall interaction point of view, a good match is evidenced with the pressure imprints on the wall from the previously published experimental result and that predicted by the current model. The numerical results for different parametric variations such as vehicle speeds, vehicle-wall separation distances and a wall inclined at 10° to the ground surface have been presented. In summary, we find that for a vertical side-wall, a separation distance of 1.35 normalized by the height of the saloon car mostly revives the cars' original drag, lift, and side forces. In addition, we have numerically demonstrated that a vehicle passing closer to a wall with 10° inclination away from the vehicle's ground surface is aerodynamically advantaged when compared to a vertical wall. In the future, a potential extension to this study is possible considering various different evaluations such as, but not restricted to (a) varying wall inclinations, (b) aerodynamic distinction by evaluating various vehicle types using wall pressure imprints, (c) a dynamically moving vehicle or the wall and, (d) incorporating a fully unsteady scale resolving simulations such as LES for higher numerical accuracy.

ACKNOWLEDGEMENT

REFERENCES

[1]   Wang D, Wang B, Chen A. Vehicle-induced aerodynamic loads on highway sound barriers part1: field experiment. Wind and Structures 2013a; 17: 435-449.

[2]   Cali PM, Covert EE. Experimental measurements of the loads induced on an overhead highway sign structure by vehicle-induced gusts. Journal of Wind Engineering and Industrial Aerodynamics 2000; 84: 87-100.

[3]   Quinn AD, Baker CJ, Wright NG. Wind and vehicle induced forces on flat plates-Part 1: Wind induced force. Journal of Wind Engineering and Industrial Aerodynamics 2001a; 89: 817-829.

[4]   Quinn AD, Baker CJ, Wright NG. Wind and vehicle induced forces on flat plates-Part 2: Vehicle induced force. Journal of Wind Engineering and Industrial Aerodynamics 2001b; 89: 831-847.

[5]   Wallis S, Quinlan W. A discussion of aerodynamic interference effects between a race car and a race track retaining wall (a wind tunnel NASCAR case study). SAE Technical Paper 1988; 880458: doi:10.4271/880458.

[6]   Strachan R, Knowles K, Lawson NJ, Finnis MV. Force and moment measurements for a generic car model in proximity to a side wall. Proceedings of the Institution of Mechanical Engineers. Part D: Journal of Automobile Engineering 2012; 226(10): 1352-1364.

[7]   Ahmed S, Ramm G, Faltin G. Some salient features of the time-averaged ground vehicle wake. SAE Technical Paper 1984; 840300: doi: 10.4271/840300.

[8]   Lichtneger P, Ruck B. Full scale experiments on vehicle induced transient loads on roadside walls. Journal of Wind Engineering and Industrial Aerodynamics 2018; 174: 451-457.

[9]   Strachan RK. The aerodynamic interference effects of side wall proximity on a generic car model. Ph.D. thesis, Cranfield University 2006; Cranfield, Bedfordshire, UK. https://dspace.lib.cranfield.ac.uk/handle/1826/4643.

[10]   Advantage CFD. A CFD NASCAR case study into the effects of wall proximity", Race Car Engineering Jun 2001; pp 48-54.

[11]   Wang D, Wang B, Chen A. Vehicle-induced aerodynamic loads on highway sound barriers part2: numerical and theoretical investigation. Wind and Structures 2013b; 17: 479-494.

[12]   Uddin M, Mallapragada S, Misar, A. Computational investigations on the aerodynamics of a generic car model in proximity to a side-wall. SAE Technical Paper 2018; 2018-01-0704: doi: 10.4271/2018-01-0704.

[13]   the-blueprints.com. Retrieved from Volkswagen Passat, https://www.the-blueprints.com/blueprints/cars/vw/68515/view/volkswagen_passat_2015/, 2015.

[14]   Evstafyeva O, Morgans A, Dalla Longa L. Simulation and feedback control of the ahmed body flow exhibiting symmetry breaking behaviour, Journal of Fluid Mechanics 2017; 817: 1–12.

[15]   Guilmineau E, Deng GB, Leroyoer A, Quetey P, Visonneau M, Wackers, J.Assessment of hybrid RANS-LES formulations for flow simulation around the Ahmed body. Computers and Fluids 2018; 176: 302-319.

[16]   Altinisik A, Kutukceken E, Umur H. Experimental and numerical aerodynamic analysis of a passenger car: influence of the blockage ratio on drag coefficient. Journal of Fluids Engineering 2015; 137: 081104.

[17]   Taherkhani AR, Gilkeson C, Gaskell P, Hewson R, Toropov V, Rezaienia A, Thompson H. Aerodynamic cfd based optimization of police car using Bezier curves, SAE International Journal of Materials and Manufacturing 2017; 10(2): 2017–01–9450, doi: 10.4271/2017-01-9450.

[18]   Yuan Z, Gu Z, Wang Y, Huang Z. Numerical investigation for the influence of the car underbody on aerodynamic force and flow structure evolution in crosswind. Advances in Mechanical Engineering 2018; 10(10): 1-14.

[19]   Lee S, Park Y, Kim J. An evaluation of factors influencing drag coefficient in double-deck tunnels by CFD simulations using factorial design method. Journal of Wind Engineering and Industrial Aerodynamics 2018; 180: 156-167.

[20]   Car body design. Retrieved from:https://www.carbodydesign.com/archive/2008/01/16-volkswagen-passat-cc/, 2008.

[21]   Kounenis C, Bonitz S, Ljungskog E, Sims-Williams D. et al., Investigations of the rear-end flow structures on a sedan car, 2016; SAE Technical Paper 2016-01-1606: doi: 10.4271/2016-01-1606.

[22]   Heft A, Indinger T, Adams N. Introduction of a New Realistic Generic Car Model for Aerodynamic Investigations. SAE Technical Paper 2012; 2012-01-0168: doi: 10.4271/2012-01-0168.

[23]   Hucho W-H, Sovran G. Aerodynamics of road vehicles. Annual Review of Fluid Mechanics 1993; 25: 485-537.

[24]   Jadon V, Agawane G, Baghel A, et al. An experimental and multiphysics based numerical study to predict automotive fuel tank sloshing noise. SAE technical paper 2014; doi:10.4271/2014-01-0888.

[25]   Viswanathan H, Awasthi A, Ageorges C, and Bohl, M. Shock Waves in Canister Purge Valves. SAE Technical Paper, 2013; doi:10.4271/2013-26-0040.